AGU ADVANCING EARTH AND SPACE SCIENCE

Geophysical Research Letters®

RESEARCH LETTER
10.1029/2021GL094937

Key Points:

- The July 2020 *M*w 7.8 Shumagin (Alaska) earthquake generated anomalously long-period tsunami waves relative to its magnitude
- The long-period tsunami was caused by the initial displacement occurring on the broad and shallow continental shelf
- Long-period tsunamis are rarely found and can be uniquely attributed to the geological setting of the Aleutian subduction zone

Supporting Information:

Supporting Information may be found in the online version of this article.

Correspondence to:

I. E. Mulia,
iyan.mulia@riken.jp;
iyan.e.m@gmail.com

Citation:

Mulia, I. E., Heidarzadeh, M., & Satake, K. (2022). Effects of depth of fault slip and continental shelf geometry on the generation of anomalously long-period tsunami by the July 2020 *M*w 7.8 Shumagin (Alaska) earthquake. *Geophysical Research Letters*, *49*, e2021GL094937. https://doi.org/10.1029/2021GL094937

Received 20 JUN 2021
Accepted 26 JAN 2022

Effects of Depth of Fault Slip and Continental Shelf Geometry on the Generation of Anomalously Long-Period Tsunami by the July 2020 *M*w 7.8 Shumagin (Alaska) Earthquake

Iyan E. Mulia[1,2], Mohammad Heidarzadeh[3], and Kenji Satake[4]

[1]Prediction Science Laboratory, RIKEN Cluster for Pioneering Research, Kobe, Japan, [2]Disaster Resilience Science Team, RIKEN Center for Advanced Intelligence Project, Tokyo, Japan, [3]Department of Civil & Environmental Engineering, Brunel University London, London, UK, [4]Earthquake Research Institute, The University of Tokyo, Tokyo, Japan

Abstract The July 2020 *M*w 7.8 Shumagin earthquake occurred in the seismic gap region along the Aleutian subduction zone. This interplate earthquake generated a small tsunami, but with unusual long-period waves ranging between 40 and 90 min. We examined the cause of such an anomalous ocean wave through a source modeling inverted from tsunami and geodetic data. Our model indicates that the plate-boundary rupture area was confined at depths of 20–40 km, although the slip resolvability decreases with depth. The coseismic seafloor displacement predominantly took place on the shallow continental shelf. Therefore, the initial water surface displacement at a mean water depth of ~200 m is responsible for the long-period waves, because tsunami period is inversely proportional to the square root of water depth. Furthermore, tsunami modeling implies that slip shallower than 20 km depth in the Aleutians would displace the seafloor beyond the continental shelf and generate shorter tsunami periods.

Plain Language Summary The tsunami generated by the July 2020 *M*w 7.8 Shumagin earthquake exhibited extremely long-period waves approximately ~60 min on average, which is much longer compared with a larger event such as the 2011 *M*w 9.0 Tohoku-oki earthquake that produced tsunami wave periods of less than 30 min. We investigated the cause of such a rare occurrence by modeling the tsunami source using both tsunami and static Global Navigation Satellite System displacements data. Our source model shows that the slip on the plate interface was confined at depths of 20–40 km, resulting in coseismic displacement at shallow water depths on the broad continental shelf extending ~150 km offshore, due to the unique continental shelf geometry of the region. Therefore, such a large ratio of long wavelength of displacement to small tsunami velocity determined by the shallow water depth would naturally induce long-period waves. From examinations of other major subduction zones globally, we found that the long-period tsunami is a unique signature attributed to the Aleutian subduction zone.

1. Introduction

The Aleutian subduction zone is characterized by the underthrusting Pacific Plate beneath the North American Plate (Figure 1). Large and great megathrust earthquakes had occurred in the region, and some of them were tsunamigenic such as the 1938 Semidi earthquake (Johnson & Satake, 1994), the 1946 Aleutian Islands earthquake (Johnson & Satake, 1997; Okal et al., 2003), and the 1964 Alaska earthquake (Ichinose et al., 2007; Johnson et al., 1996). On 22 July 2020, a large *M*w 7.8 earthquake ruptured the Shumagin gap, a seismically inactive area compared to other regions along the Alaska-Aleutian arc (Sykes, 1971). The US Geological Survey National Earthquake Information Center (USGS-NEIC) estimated the earthquake origin time as 06:12:44 UTC and the hypocenter at 158.554°W, 55.068°N with a depth of 28 km (https://earthquake.usgs.gov/earthquakes/eventpage/us7000asvb/executive). It was located slightly to the east of the 1917 *M*w 7.4 earthquake (Estabrook & Boyd, 1992), although still within the same segment. The rupture was bounded on the east by the west edge of the great 1938 *M*w 8.2 Semidi earthquake that generated a Pacific-wide tsunami (Johnson & Satake, 1994; Okal, 1992). Further to the west of the July 2020 Shumagin event, the 1946 Aleutian earthquake of magnitude *M*w 8.6 (Johnson & Satake, 1997; López & Okal, 2006) also induced a tsunami with a more devastating impact resulting in an extreme run-up height of approximately 40 m and far-field tsunami damage in Hawaii and Marquesas (Okal et al., 2003). Considering that the Aleutian subduction zone poses an immense future earthquake and tsunami hazard, it is important to understand the underlying physical process of each event occurring in the region.

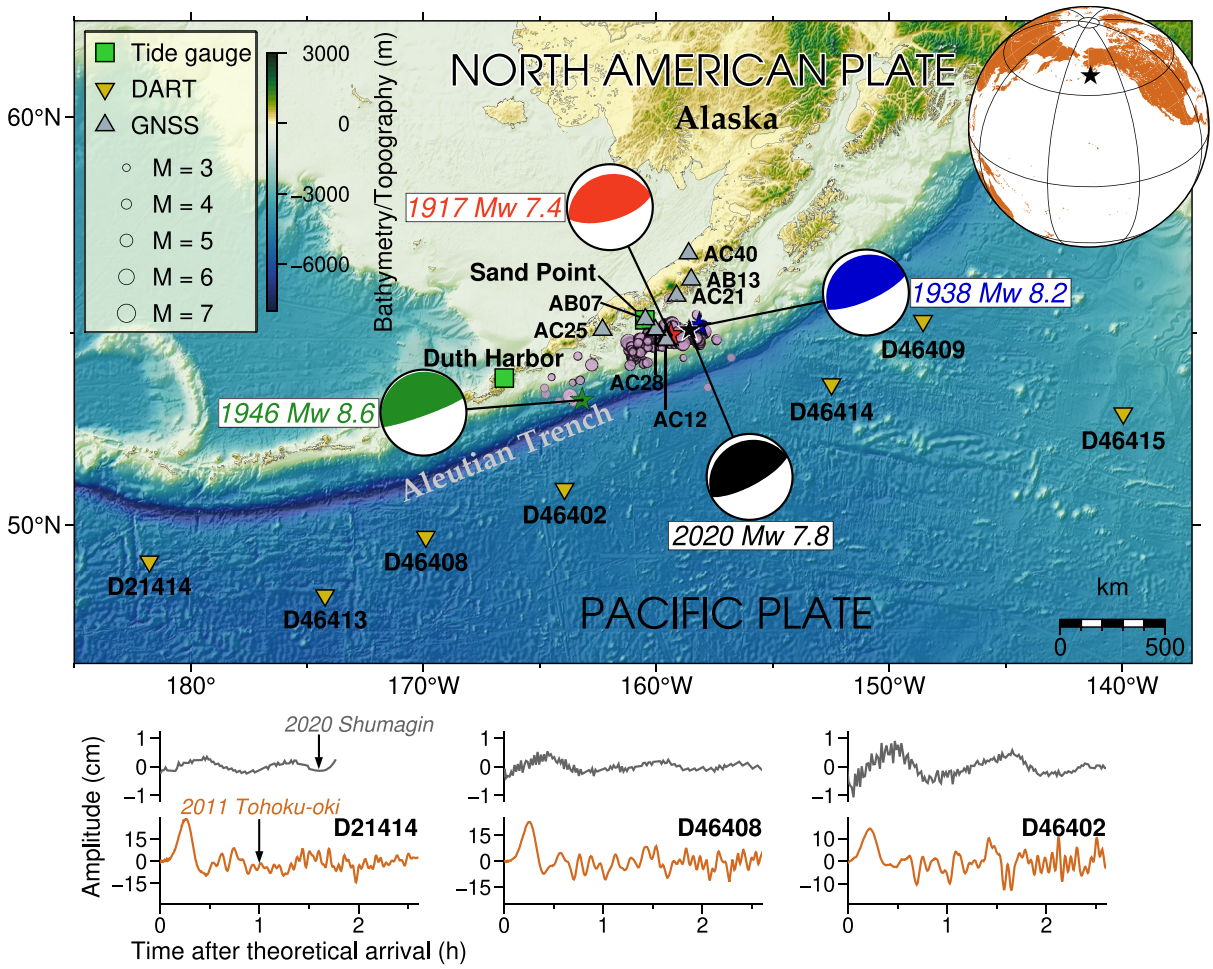

Figure 1. Top figure indicates bathymetry/topography map overlaid with locations of the tsunami and geodetic observations, and 1-month USGS-NEIC aftershock distribution. Stars are epicenters of the 2020 (Global Centroid Moment Tensor, black), 1946 (Johnson & Satake, 1997, green), 1938 (Okal, 1992, blue), and 1917 (Estabrook & Boyd, 1992, red) earthquakes with the corresponding focal mechanisms. Bottom figures show samples of tsunami observations from the 2011 Tohoku-oki and 2020 Shumagin events at three DART buoys (unfiltered), with time axis starting at respective theoretical arrival times.

Recent studies have delineated the source mechanism of the July 2020 Shumagin earthquake using both static and high-rate GNSS displacements, strong-motion velocities, regional broadband records, and teleseismic body waves (Crowell & Melgar, 2020; Liu et al., 2020; Ye et al., 2021). Here, we introduce an additional insight from the tsunami genesis perspective. The July 2020 Shumagin earthquake generated unusual long-period tsunami waves surprisingly longer than a much larger magnitude event such as the 2011 Tohoku-oki tsunami (see Figure 1, bottom panels). Larson et al. (2020) confirmed the long-period tsunami waves of 90–110 min associated with the July 2020 Shumagin earthquake from their GNSS interferometric reflectometry (GNSS-IR) observation at a GNSS station named AC12. In our previous study (Heidarzadeh & Mulia, 2021), using a simple source model with uniform slip, we attributed the long-period tsunami of the July 2020 Shumagin event to the effect of shallow water depths over the source area. Here we consider a finite fault source model to further reveal the tsunami source characteristics using a tsunami waveform inversion approach (Mulia et al., 2018; Satake, 1989). Additionally, we also utilize static displacement data at GNSS stations in the inversion to better constrain the total moment release.

2. Material and Method

We use tsunami data registered at two tide gauges at Sand Point and Dutch Harbor, as well as at seven offshore tsunami observation stations of the Deep-ocean Assessment and Reporting of Tsunamis (DART) buoys provided by the US National Oceanic and Atmospheric Administration (Figure 1). After tide removal by a polynomial fit to the water level and lowpass filtering with a cutoff period of 10 min, the data are resampled to a 15-s interval for the inversion analysis. However, as the bottom pressure sensor is installed on the seafloor, DART data is prone to seismic interference, particularly if the stations are located relatively near to the source (Saito & Kubota, 2020), which was observed in the July 2020 Shumagin event (Heidarzadeh & Mulia, 2021; Ye et al., 2021). As shown in Figure S1 in Supporting Information S1, although the seismic noise at specific frequencies can be removed by filtering, some low-frequency seismic waves persist as they share common spectral components with the tsunami signals (Saito & Kubota, 2020). For the joint inversion, we include three-component static offsets data at seven Network of Americas GNSS stations operated by the UNAVCO. The bathymetry data used in the tsunami modeling are obtained from the General Bathymetric Charts of the Oceans (GEBCO) 2020 digital grid which has a spatial resolution of 15 arc-sec (Tozer et al., 2019). We interpolate the GEBCO data into a three-level nested grid system and input it into the tsunami simulation code called JAGURS (Baba et al., 2015). The tsunami waveforms at DART buoys and tide gauges are computed at grid sizes of 60 arc-sec and 20 arc-sec, respectively.

We apply a two-step inversion in which the sea surface vertical displacement is first inverted from the tsunami waveform data, then the finite fault slip distribution is inverted in the second step from the estimated sea surface displacement (Gusman et al., 2018; Hossen et al., 2018). More specifically, we employ an Adaptive Tsunami Source Inversion that efficiently constructs the tsunami Green's function using a reciprocity principle, including optimizations of unit source locations and fault parameters (Mulia et al., 2018). However, since the uncertainty of fault parameters of megathrust earthquakes are relatively small compared to intraplate faulting, in this study, we only perform the optimization for the first step inversion.

In the first step inversion for the sea surface displacement, the reciprocal waveforms can be inaccurate when the source area is located near the land. To circumvent the problem, following the previous studies (Gusman et al., 2016; Mulia & Asano, 2015, 2016), we reconstruct the Green's function with a fixed Gaussian unit source radius of 40 km and apply a phase correction method (Watada et al., 2014) once the optimization of the first step is completed. To avoid overfitting to the tide gauge data with amplitudes of 5–20 times higher than DARTs data, based on a trial-and-error we weight the tsunami waveforms at DART buoys and tide gauges by factors of 20 and 1, respectively. The larger weight at DART buoys is also preferred because offshore tsunami observations are free from coastal effects, thus more accurately represent the tsunami source signatures.

In the second step inversion, the slip distribution on the fault plane is inverted from the resultant vertical sea surface displacement estimated in the first step (see inset of Figure 2a) and coseismic offsets at the GNSS sites. The number of data points calculated using a quadtree decomposition is 1952, which are then used together with the three-component static offsets at seven GNSS stations. We also weight the GNSS data by factors of 5–30 depending on their distances from the epicenter and double the weight for the vertical component. A spatial smoothness constraint for the slip distribution is applied through a Laplacian operator. The Global Centroid Moment Tensor (GCMT) for the event indicates a best double couple solution with strike = 242°, dip = 17°, and rake = 90° (https://www.globalcmt.org/CMTsearch.html). Here, we set the fault strike of 240° and dip of 17° referring to the plate interface of the SLAB2 model (Hayes et al., 2018). The fault has a top edge depth of 18 km, downdip width of 90 km, and along-strike length of 130 km, which is discretized into subfaults of size 10 × 10 km. Then, using Okada's co-seismic dislocation model (Okada, 1985), we construct two sets of displacement Green's functions allowing for the rake to vary on each subfault between 45° and 135°. We note that our fault size does not entirely cover the aftershock distribution west of 160°W, because previous studies demonstrated that the main slip region was confined within a smaller area in the vicinity of the Shumagin Islands (Crowell & Melgar, 2020; Liu et al., 2020; Ye et al., 2021). Moreover, compared to seismic waves, tsunami waveforms are more sensitive to the fault extent, particularly in the direction to which the main energy propagates (Heidarzadeh et al., 2017).

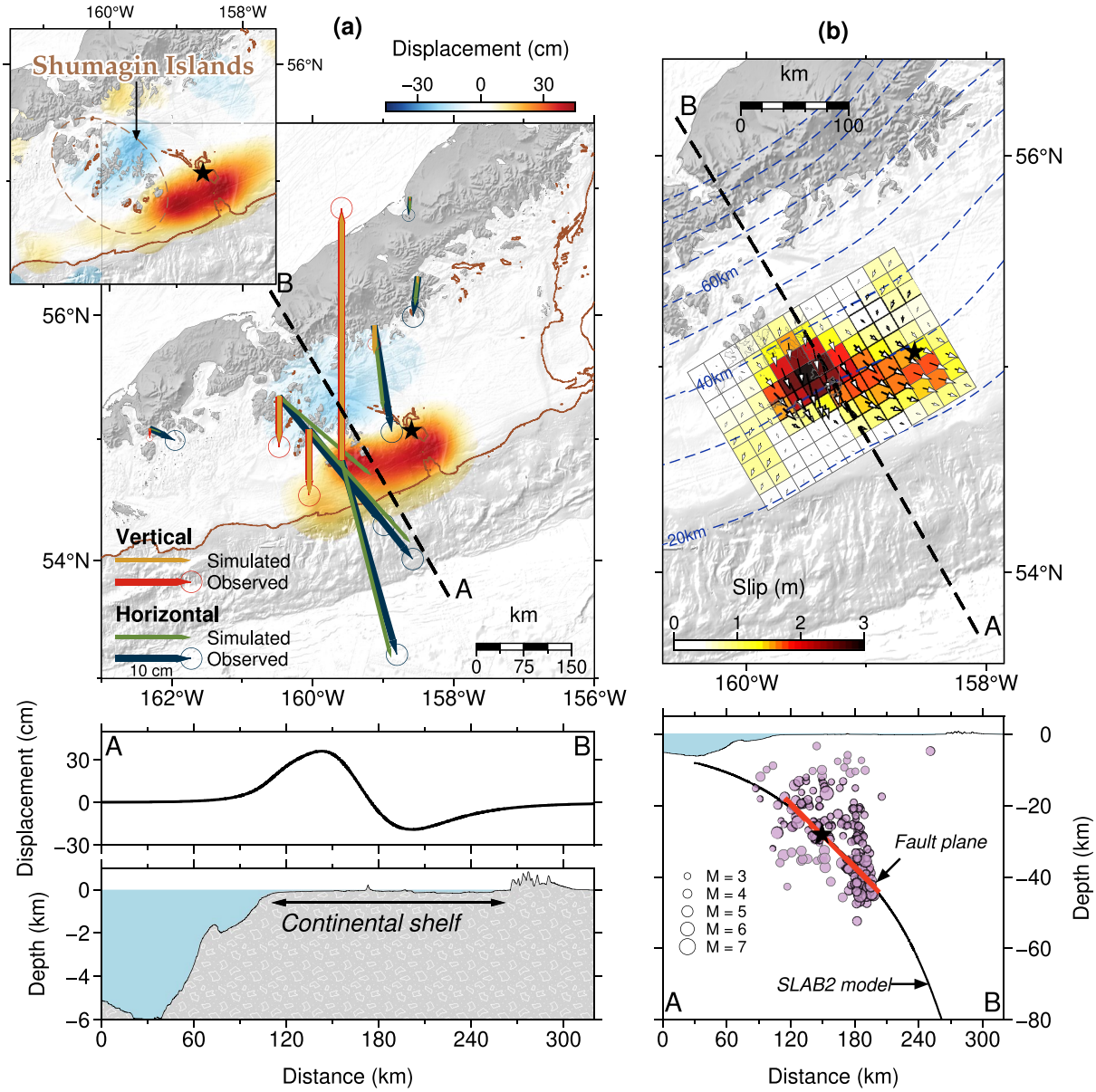

Figure 2. (a) Modeled vertical displacement calculated from the slip used to initiate the tsunami simulation and comparisons of modeled versus observed vertical and horizontal displacements at GNSS stations (top). Brown contours mark a 200 m water depth, the black star indicates the epicenter, and the inset shows the inverted sea surface displacement resulted in the first step. Cross-section of vertical displacement and water depth (bottom). (b) Inverted slip distribution and rakes (top). Dashed contours indicate plate interface depths from the SLAB2 model. Cross-section of depth, fault plane, hypocenter, and 1-month USGS-NEIC aftershocks distribution (bottom).

3. Results

Figure 2a shows our modeled initial coseismic displacements calculated from the inverted slip distribution in the second step (Figure 2b). The inset of Figure 2a depicts the inverted sea surface displacement in the first step which was used as data in the second step together with the static GNSS record. In general, the model produces reasonable agreement with the observed static GNSS displacements both vertically and horizontally. When the vertical displacement and water depth are plotted along the specified cross-section (Figure 2a, bottom panel), we can clearly see that the displacement length or tsunami source wavelength of ∼160 km with a crest-to-trough height of 45 cm occurred on the broad shallow continental shelf with a mean water depth of ∼200 m stretching approximately 150 km from the coastline. Derived from the linearized shallow water equation (Heidarzadeh & Satake, 2014), the tsunami period T can roughly be estimated using $T = \lambda/gd$, where λ is the tsunami source

wavelength, d is water depth, and g is gravitational acceleration (9.81 m/s^2). Substituting the above parameters to the equation would give an estimated period of 60.2 min. Although a slight variation of periods is expected at different stations in response to various local effects (e.g., coastal geometry, bay oscillations), this rough estimate would give a simple and general idea on how the long-period waves were generated. More detailed comparison of tsunami periods with the 2011 Tohoku-oki event was presented in Heidarzadeh and Mulia (2021).

Our slip distribution model (Figure 2b, top panel) indicates that overall, the plate-boundary slip was limited between 20 and 40 km depths with a mean slip over the entire subfaults of 0.95 m, consistent with the lack of aftershocks near the trench and deeper than 40 km (Figure 2b, bottom panel). The maximum slip of approximately 3 m occurred beneath the Shumagin Islands, which is location-wise similar to the previous studies (Crowell & Melgar, 2020; Liu et al., 2020; Ye et al., 2021). However, in our case, the main slip region is situated on the poorly resolved portion of the fault as indicated by the resolution test result (Figure S2b in Supporting Information S1). Nevertheless, our finite fault model can provide an accurate estimate of rupture updip limit which is an important factor for simulating the tsunami in this region. The same fault dimension but with a uniform slip (averaged from the finite fault solution) would overestimate the tsunami waveforms (Figure S3b in Supporting Information S1) due to the shallow slip at depth of less than ~20 km, indicating the sensitivity of tsunami data to the depth of fault slip. For the same reason, to preclude the poor simulated waveform fit to observations, a smaller fault size of 110 km in length and 70 km in width (Figure S3a in Supporting Information S1) was considered in our previous study using a uniform slip distribution (Heidarzadeh & Mulia, 2021).

Crowell and Melgar (2020) advocated that the July 2020 Shumagin earthquake did not involve rupture of the plate interface updip from a 20 km depth to the trench, which was also seen in the results of Liu et al. (2020) and Ye et al. (2021). In addition to the previous result from the uniform slip model, here we examine the updip limit of the event using tsunami simulations from the USGS-NEIC source model (Figure S4a in Supporting Information S1) that has slip patches of more than 1 m at depths of less than 20 km (Figure S4b in Supporting Information S1). The shallow slip results in displacement beyond the continental shelf at a water depth of about 2000 m (Figure S4c in Supporting Information S1) owing to the geological settings of the region where a vertical projection of ~20 km slab depth corresponds to the edge of the continental shelf (see Figure 2, bottom panels). Consequently, the computed tsunami excites higher amplitudes and shorter periods of the first wave than the observations (Figure S5 in Supporting Information S1). Our current result further postulates that the tsunami data is adequate for accurately constraining the fault dimension or the updip limit of the rupture, which has previously been demonstrated by Heidarzadeh et al. (2017).

We also perform an inversion using tsunami data only (Figure S6 in Supporting Information S1). As expected, the static offsets at GNSS stations are poorly approximated by this model, although the simulated tsunami waveforms exhibit a good fit to the observations. Assuming a rigidity of 4.3×10^{10} N/m^2 (Sallarès & Ranero, 2019), the seismic moment of this slip model is calculated as 3.5×10^{20} N m (Mw 7.63) considerably smaller than that from seismically estimated moment magnitude of Mw 7.84 (e.g., Liu et al., 2020). Incorporating the static GNSS data in the inversion facilitates to constrain deformation occurring inland, thus leads to a better estimation of total moment release of 4.77×10^{20} N m (Mw 7.72). However, the static GNSS data does not improve the resolvability of the inverted slip as shown in Figure S2c in Supporting Information S1 due to the limited number of stations and coverage. Furthermore, the contribution of static offsets data to model the fault slip is restricted to a specific depth and distance between offshore slip and GNSS instruments (Williamson & Newman, 2018). Full high-rate GNSS waveforms preferably complemented by seismic data are needed to better resolve the slip, particularly in the deeper parts of the plate boundary (Crowell & Melgar, 2020).

Comparisons of observed against simulated tsunami waveforms using the initial condition from the slip-based calculated displacement, depicted in Figure 2a, are shown in Figure 3. The dominant tsunami periods at tide gauges vary within the range of 40–60 min, which are relatively shorter than at DART stations (Figure 3, right panel). The largest tsunami amplitude of ~24 cm was observed at Sand Point and accurately reproduced by our source model. As shown in Figure S3b in Supporting Information S1, the tsunami at this station was overestimated by our previous study using a uniform slip model (Heidarzadeh & Mulia, 2021) signifying the sensitivity of near-field tsunami to the slip distribution. At Dutch Harbor, the agreement between observed and simulated tsunami is not perfect which is most likely due to bathymetry effects of the bay/harbor that are not well-represented in our numerical grid resolution (Figure S7 in Supporting Information S1).

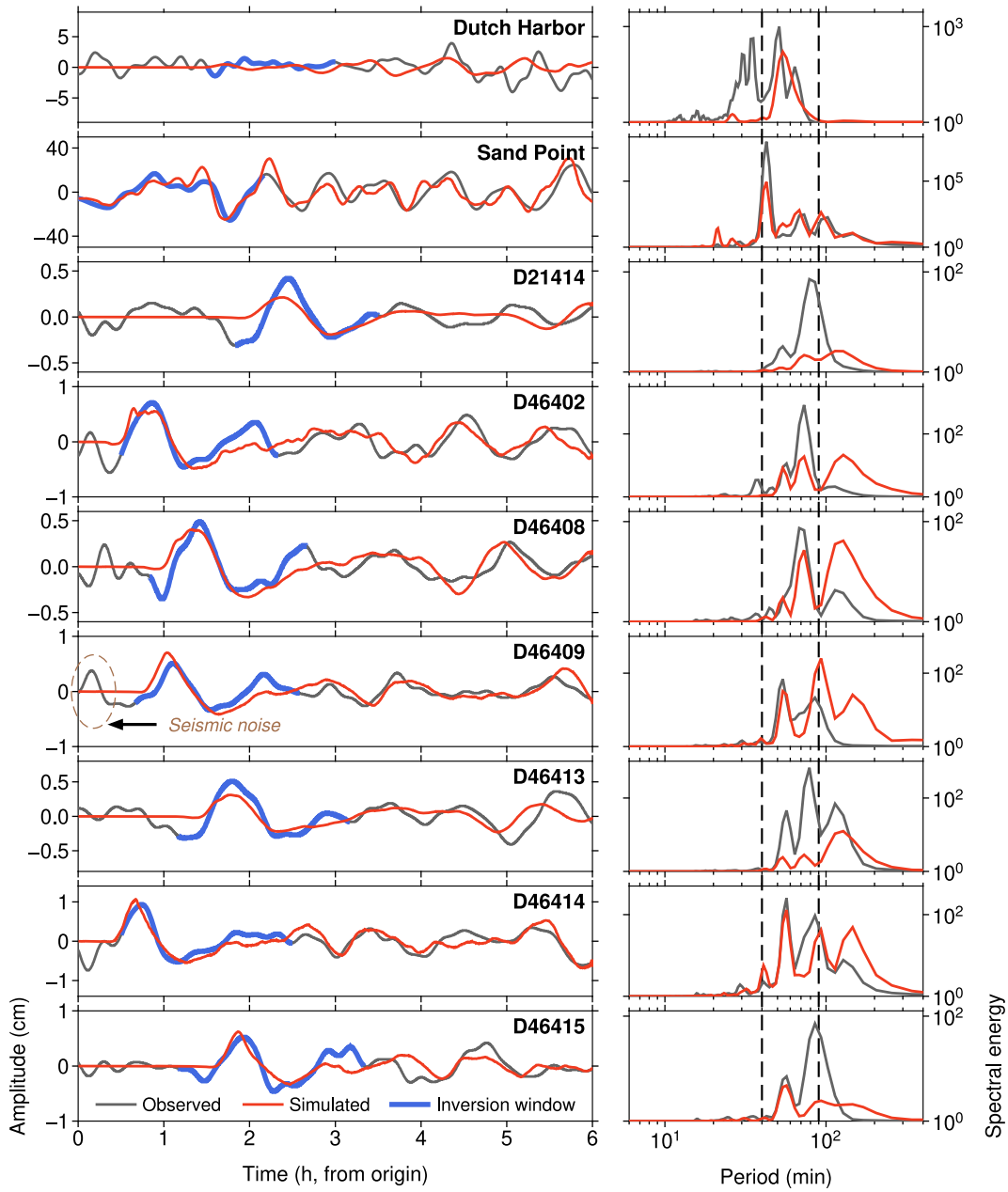

Figure 3. Comparisons of observed and simulated tsunami waveforms in time (left panel) and frequency (right panel) domains.

The nearest DART buoy (D46414) to the source registered the largest amplitude among other stations of ~1 cm. At this location as well as other nearby stations, low-frequency seismic signals that cannot be removed by filtering, appears in the early stages of the time series. Fortunately, such noisy signals occur outside the data time window, thus have no or minor effects on the inversion. Overall, the match of simulation results with observations is nearly perfect at most of DART buoys. Although there are some disagreements in the spectral amplitude, the dominant long tsunami periods of 50–90 min can also be identified in the simulated waveforms. We also notice subtle early arrivals at a few stations (e.g., D21414, D46408, and D40409), which are unlikely caused by the dispersive effect because we employ a phase correction method (Watada et al., 2014), and the tsunami arrival discrepancy is not very apparent in the inversion result using tsunami data only (Figure S6 in Supporting Information S1). The joint inversion with GNSS data slightly alters the initial vertical displacement, which in turn

affects the simulated waveforms. Nonetheless, the joint inversion result is preferable as it represents the balance of fit between tsunami and GNSS data.

Additionally, we also plot the simulated tsunami waveform in the vicinity of the AC12 GNSS station (Figure S8 in Supporting Information S1). There are two distinct dominant tsunami periods of 64 and 114 min which are comparable to the observed GNSS-IR-based sea level by Larson et al. (2020) with dominant periods of 90 and 110 min. Therefore, the July 2020 Shumagin tsunami clearly demonstrated extremely long-period waves compared to earthquakes of similar magnitude such as the 2012 Haida Gwaii (Gusman et al., 2016) and 2016 Kaikoura (Heidarzadeh et al., 2019) events that generated tsunamis with periods of only 15–20 min. The tsunami period by the July 2020 Shumagin earthquake is even longer than a much larger event of the 2011 Tohoku-oki tsunami (Figure 1). Based on local tide gauge records, Tanioka et al. (2019) found that, irrespective of the bay resonance and edge waves influence, the 2011 Tohoku-oki tsunami had a period of 25–28 min.

4. Discussion

Although the Shumagin segment is categorized as a weakly locked zone (Li & Freymueller, 2018), we may not rule out the possibility of future shallow megathrust tsunamigenic events as the coupling model at this portion is poorly constrained by the onshore data. A recent study by Lindsey et al. (2021) suggested that their new model can reveal higher slip rate deficits at the trench compared to previous studies, which implies that the current understanding of megathrust tsunami hazards globally may have been underestimated. There was also evidence that weakly locked or even creeping plate boundary sections could host tsunamigenic earthquakes (Bilek & Engdahl, 2007; Satake, 1994). Such a hazardous shallow slip was exemplified by the 1946 tsunami earthquake (Johnson & Satake, 1997; Kanamori, 1972) occurring on the adjacent segment where creeping is identified as the dominant mode of the subduction (Li & Freymueller, 2018). Furthermore, from seismic reflection imaging, Bécel et al. (2017) found that the near-trench portion of the Shumagin gap consists of heterogeneous plate interfaces, deformed sediment, and splay faults that are capable of inducing tsunamigenic earthquakes. However, hints suggesting whether the Shumagin gap can host great ($M_w > 8$) earthquakes and tsunamis remain debated.

The main contributing factor to the long-period tsunami of the event, besides the initial displacement extent, is the geometry of the continental shelf which is considerably broader compared to that of other world's major subduction zones typically characterized by shallow submarine terrace distance of less than 100 km from the shoreline. Figures 4a–4d show that a 20 km depth of megathrust interfaces in the Japan trench, Sunda trench, and northern Peru-Chile trench corresponds to ∼2000 m water depth on the top. Therefore, in these regions, fault slip confined within the same depths as the July 2020 Shumagin earthquake (20–40 km) would produce shorter tsunami period. In the Cascadia subduction zone (Figure 4b), however, a shallow megathrust interface at depths of approximately between 15 and 22 km is located right under the continental shelf. This resembles the Shumagin gap, but the length of the continental shelf from the shoreline is only about 80 km, thus large earthquakes within the aforementioned range of depths would likely displace a substantial portion of deeper seafloor or continental slope. Therefore, the long-period tsunami can be a unique signature attributed to the Aleutian subduction zone, particularly in the Shumagin gap and to the northeast of the segment exhibiting a broader continental shelf (Figure S9 in Supporting Information S1).

5. Conclusion

The Shumagin gap is characterized by a broad continental shelf extending ∼150 km from shoreline, which is considerably wider than other world's major subduction systems. Based on our source modeling, we find that this unique feature was responsible for the extremely long-period tsunamis ranging between 40 and 90 min excited by the July 2020 *M*w 7.8 Shumagin earthquake, which is unusual for an event of such a magnitude. The geometry of the continental shelf in this region translated a confined slip occurred at depths between 20 and 40 km on the plate interface into a significant portion of approximately 160 km coseismic displacements on the shallow submarine terrace with a mean water depth of ∼200 m. Consequently, such a setting and long-wave feature produced long-period tsunami waves. Additionally, our tsunami simulation confirms that shallow slip at depths of less than 20 km was unlikely to be associated with the earthquake because it would generate considerably shorter tsunami periods than observations. This could indicate that if strain is build-up on the near-trench section, it would

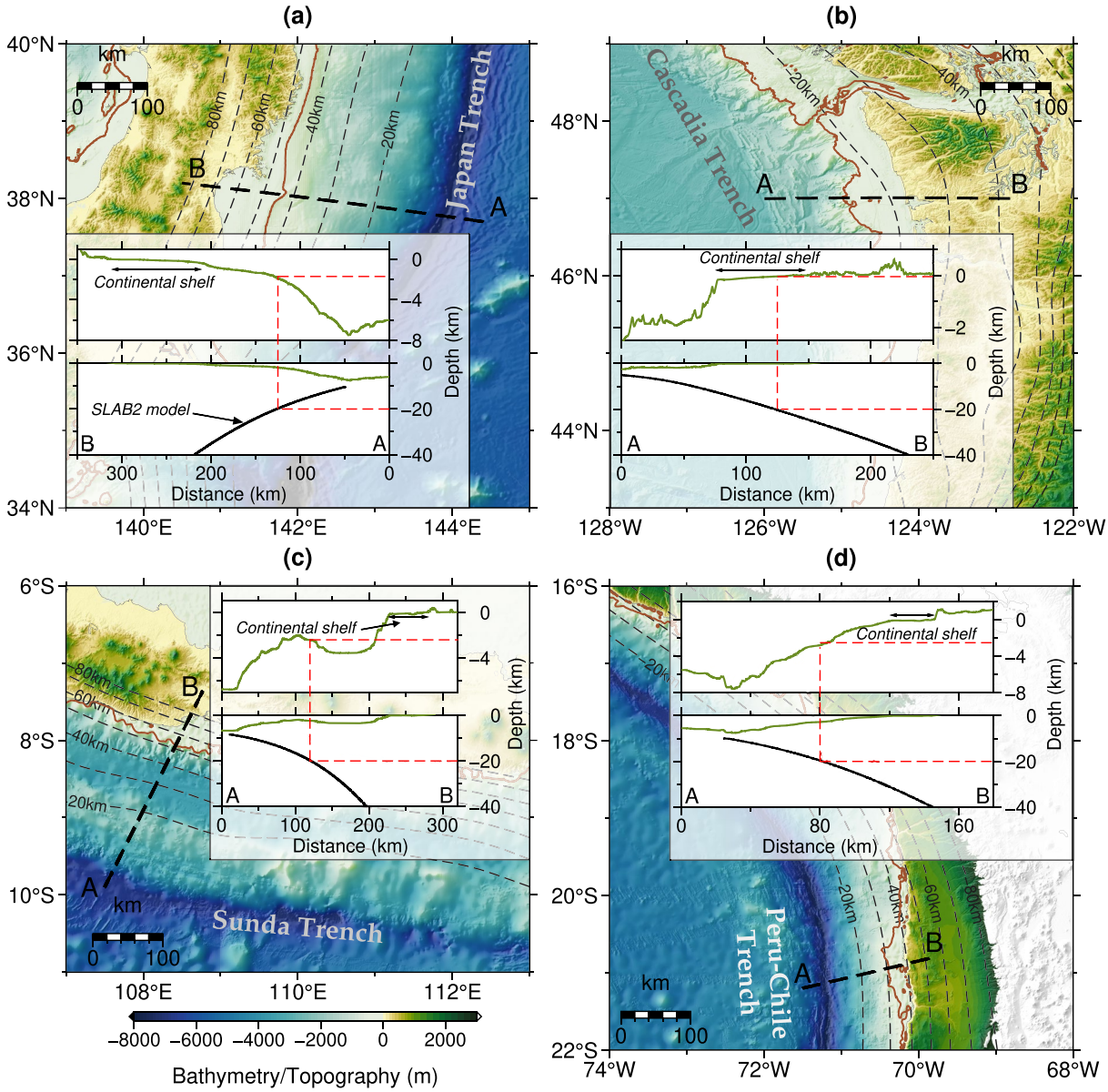

Figure 4. Geological settings of the worldwide major subduction zones. Brown contours mark a 200 m water depth and dashed contours show plate interface depths from the SLAB2 model. Insets depict projections from a 20 km slab depth, indicated by red dashed lines, to the surface (green lines). (a) Japan trench. (b) Cascadia trench. (c) Sunda trench. (d) Northern Peru-Chile trench.

generate future tsunamis. Major tsunami hazard from shallow earthquakes should be anticipated, particularly since the degree of interface coupling near the trench is still poorly constrained by the present onshore data.

Data Availability Statement

The tide gauge data for Sand Point (http://www.ioc-sealevelmonitoring.org/station.php?code=sdpt) and Dutch Harbor (http://www.ioc-sealevelmonitoring.org/station.php?code=dutc) are provided by the Sea Level Station Monitoring Facility of the Intergovernmental Oceanographic Commission of the United Nations. The DART data of the United States National Oceanic and Atmospheric Administration's were downloaded from https://www.ndbc.noaa.gov/obs.shtml. Static GNSS displacements were obtained from the UNAVCO Bulletin Board (https://www.unavco.org/highlights/2020/simeonof.html). Bathymetric data are based on GEBCO 2020 Grid available at

https://www.gebco.net/data_and_products/gridded_bathymetry_data/. All figures were produced using the GMT software (Wessel & Smith, 1991).

Acknowledgments
The work is part of the RIKEN Pioneering Project "Prediction for Science." M. Heidarzadeh is funded by the Royal Society (The United Kingdom), Grant No. CHL\R1\180173.

References

Baba, T., Takahashi, N., Kaneda, Y., Ando, K., Matsuoka, D., & Kato, T. (2015). Parallel implementation of dispersive tsunami wave modeling with a nesting algorithm for the 2011 Tohoku tsunami. *Pure and Applied Geophysics*, *172*(12), 3455–3472. https://doi.org/10.1007/s00024-015-1049-2

Bécel, A., Shillington, D. J., Delescluse, M., Nedimović, M. R., Abers, G. A., Saffer, D. M., et al. (2017). Tsunamigenic structures in a creeping section of the Alaska subduction zone. *Nature Geoscience*, *10*(8), 609–613. https://doi.org/10.1038/ngeo2990

Bilek, S. L., & Engdahl, E. R. (2007). Rupture characterization and aftershock relocations for the 1994 and 2006 tsunami earthquakes in the Java subduction zone. *Geophysical Research Letters*, *34*(20). https://doi.org/10.1029/2007GL031357

Crowell, B. W., & Melgar, D. (2020). Slipping the Shumagin gap: A kinematic coseismic and early afterslip model of the *M*w 7.8 simeonof island, Alaska, earthquake. *Geophysical Research Letters*, *47*(19), e2020GL090308. https://doi.org/10.1029/2020GL090308

Estabrook, C. H., & Boyd, T. M. (1992). The Shumagin Islands, Alaska, earthquake of 31 May 1917. *Bulletin of the Seismological Society of America*, *82*(2), 755–773.

Gusman, A. R., Mulia, I. E., & Satake, K. (2018). Optimum sea surface displacement and fault slip distribution of the 2017 Tehuantepec earthquake (*M*w 8.2) in Mexico estimated from tsunami waveforms. *Geophysical Research Letters*, *45*(2). https://doi.org/10.1002/2017GL076070

Gusman, A. R., Mulia, I. E., Satake, K., Watada, S., Heidarzadeh, M., & Sheehan, A. F. (2016). Estimate of tsunami source using optimized unit sources and including dispersion effects during tsunami propagation: The 2012 Haida Gwaii earthquake. *Geophysical Research Letters*, *43*(18). https://doi.org/10.1002/2016GL070140

Hayes, G. P., Moore, G. L., Portner, D. E., Hearne, M., Flamme, H., Furtney, M., & Smoczyk, G. M. (2018). Slab2, a comprehensive subduction zone geometry model. *Science*, *362*(6410), 58–61. https://doi.org/10.1126/science.aat4723

Heidarzadeh, M., & Mulia, I. E. (2021). Ultra-long period and small-amplitude tsunami generated following the July 2020 Alaska *M*w 7.8 Tsunamigenic earthquake. *Ocean Engineering*, *234*, 109243. https://doi.org/10.1016/j.oceaneng.2021.109243

Heidarzadeh, M., Murotani, S., Satake, K., Takagawa, T., & Saito, T. (2017). Fault size and depth extent of the Ecuador earthquake (*M*w 7.8) of 16 April 2016 from teleseismic and tsunami data. *Geophysical Research Letters*, *44*(5), 2211–2219. https://doi.org/10.1002/2017GL072545

Heidarzadeh, M., & Satake, K. (2014). Possible sources of the tsunami observed in the northwestern Indian Ocean following the 2013 September 24 *M*w 7.7 Pakistan inland earthquake. *Geophysical Journal International*, *199*(2), 752–766.

Heidarzadeh, M., Tappin, D. R., & Ishibe, T. (2019). Modeling the large runup along a narrow segment of the Kaikoura coast, New Zealand following the November 2016 tsunami from a potential landslide. *Ocean Engineering*, *175*, 113–121. https://doi.org/10.1016/j.oceaneng.2019.02.024

Hossen, M. J., Gusman, A., Satake, K., & Cummins, P. R. (2018). An adjoint sensitivity method applied to time reverse imaging of tsunami source for the 2009 Samoa earthquake. *Geophysical Research Letters*, *45*(2), 627–636. https://doi.org/10.1002/2017GL076031

Ichinose, G., Somerville, P., Thio, H. K., Graves, R., & O'Connell, D. (2007). Rupture process of the 1964 Prince William Sound, Alaska, earthquake from the combined inversion of seismic, tsunami, and geodetic data. *Journal of Geophysical Research*, *112*(B7). https://doi.org/10.1029/2006JB004728

Johnson, J. M., & Satake, K. (1994). Rupture extent of the 1938 Alaskan earthquake as inferred from tsunami waveforms. *Geophysical Research Letters*, *21*(8), 733–736. https://doi.org/10.1029/94GL00333

Johnson, J. M., & Satake, K. (1997). Estimation of seismic moment and slip distribution of the April 1, 1946, Aleutian tsunami earthquake. *Journal of Geophysical Research*, *102*(B6), 11765–11774. https://doi.org/10.1029/97JB00274

Johnson, J. M., Satake, K., Holdahl, S. R., & Sauber, J. (1996). The 1964 Prince William Sound earthquake: Joint inversion of tsunami and geodetic data. *Journal of Geophysical Research*, *101*(B1), 523–532. https://doi.org/10.1029/95JB02806

Kanamori, H. (1972). Mechanism of tsunami earthquakes. *Physics of the Earth and Planetary Interiors*, *6*(5), 346–359.

Larson, K. M., Lay, T., Yamazaki, Y., Cheung, K. F., Ye, L., Williams, S. D. P., & Davis, J. L. (2020). Dynamic sea level variation from GNSS: 2020 Shumagin earthquake tsunami resonance and hurricane laura. *Geophysical Research Letters*, *48*, e2020GL091378. https://doi.org/10.1029/2020GL091378

Li, S., & Freymueller, J. T. (2018). Spatial variation of slip behavior beneath the Alaska Peninsula along Alaska-Aleutian subduction zone. *Geophysical Research Letters*, *45*(8), 3453–3460. https://doi.org/10.1002/2017GL076761

Lindsey, E. O., Mallick, R., Hubbard, J. A., Bradley, K. E., Almeida, R. V., Moore, J. D. P., et al. (2021). Slip rate deficit and earthquake potential on shallow megathrusts. *Nature Geoscience*, *14*(5), 321–326. https://doi.org/10.1038/s41561-021-00736-x

Liu, C., Lay, T., Xiong, X., & Wen, Y. (2020). Rupture of the 2020 *M*W 7.8 earthquake in the Shumagin gap inferred from seismic and geodetic observations. *Geophysical Research Letters*, *47*(22), e2020GL090806. https://doi.org/10.1029/2020GL090806

López, A. M., & Okal, E. A. (2006). A seismological reassessment of the source of the 1946 Aleutian 'tsunami' earthquake. *Geophysical Journal International*, *165*(3), 835–849. https://doi.org/10.1111/j.1365-246X.2006.02899.x

Mulia, I. E., & Asano, T. (2015). Randomly distributed unit sources to enhance optimization in tsunami waveform inversion. *Natural Hazards and Earth System Sciences*, *15*(1). https://doi.org/10.5194/nhess-15-187-2015

Mulia, I. E., & Asano, T. (2016). Initial tsunami source estimation by inversion with an intelligent selection of model parameters and time delays. *Journal of Geophysical Research: Oceans*, *121*(1). https://doi.org/10.1002/2015JC010877

Mulia, I. E., Gusman, A. R., Jakir Hossen, M., & Satake, K. (2018). Adaptive tsunami source inversion using optimizations and the reciprocity principle. *Journal of Geophysical Research: Solid Earth*, *123*(12), https://doi.org/10.1029/2018JB016439

Okada, Y. (1985). Internal deformation due to shear and tensile faults in a half-space. *Bulletin of the Seismological Society of America*, *82*(2), 1018–1040.

Okal, E. A. (1992). Use of the mantle magnitude Mm for the reassessment of the moment of historical earthquakes. *Pure and Applied Geophysics*, *139*(1), 59–85. https://doi.org/10.1007/BF00876826

Okal, E. A., Plafker, G., Synolakis, C. E., & Borrero, J. C. (2003). Near-field survey of the 1946 aleutian tsunami on unimak and sanak Islands. *Bulletin of the Seismological Society of America*, *93*(3), 1226–1234. https://doi.org/10.1785/0120020198

Saito, T., & Kubota, T. (2020). Tsunami modeling for the Deep Sea and inside focal areas. *Annual Review of Earth and Planetary Sciences*, *48*(1), 121–145. https://doi.org/10.1146/annurev-earth-071719-054845

Sallarès, V., & Ranero, C. R. (2019). Upper-plate rigidity determines depth-varying rupture behaviour of megathrust earthquakes. *Nature*, *576*(7785), 96–101. https://doi.org/10.1038/s41586-019-1784-0

Satake, K. (1989). Inversion of tsunami waveforms for the estimation of heterogeneous fault motion of large submarine earthquakes: The 1968 Tokachi-oki and 1983 Japan Sea earthquakes. *Journal of Geophysical Research*, *94*(B5), 5627–5636. https://doi.org/10.1029/JB094iB05p05627

Satake, K. (1994). Mechanism of the 1992 Nicaragua tsunami earthquake. *Geophysical Research Letters*, *21*(23), 2519–2522. https://doi.org/10.1029/94GL02338

Sykes, L. R. (1971). Aftershock zones of great earthquakes, seismicity gaps, and earthquake prediction for Alaska and the Aleutians. *Journal of Geophysical Research*., *76*(32), 8021–8041. https://doi.org/10.1029/JB076i032p08021

Tanioka, Y., Shibata, M., Yamanaka, Y., Gusman, A. R., & Ioki, K. (2019). Generation mechanism of large later phases of the 2011 Tohoku-oki tsunami causing damages in Hakodate, Hokkaido, Japan. *Progress in Earth and Planetary Science*, *6*(1), 30. https://doi.org/10.1186/s40645-019-0278-x

Tozer, B., Sandwell, D. T., Smith, W. H. F., Olson, C., Beale, J. R., & Wessel, P. (2019). Global bathymetry and topography at 15 arc sec: SRTM15+. *Earth and Space Science*, *6*(10), 1847–1864. https://doi.org/10.1029/2019EA000658

Watada, S., Kusumoto, S., & Satake, K. (2014). Traveltime delay and initial phase reversal of distant tsunamis coupled with the self-gravitating elastic Earth. *Journal of Geophysical Research: Solid Earth*, *119*(5), 4287–4310. https://doi.org/10.1002/2013JB010841

Wessel, P., & Smith, W. H. F. (1991). Free software helps map and display data. *Eos, Transactions American Geophysical Union*, *72*(41), 441–446. https://doi.org/10.1029/90EO00319

Williamson, A. L., & Newman, A. V. (2018). Limitations of the resolvability of finite-fault models using static land-based geodesy and open-ocean tsunami waveforms. *Journal of Geophysical Research: Solid Earth*, *123*(10), 9033–9048. https://doi.org/10.1029/2018JB016091

Ye, L., Lay, T., Kanamori, H., Yamazaki, Y., & Cheung, K. F. (2021). The 22 July 2020 *M*W 7.8 Shumagin seismic gap earthquake: Partial rupture of a weakly coupled megathrust. *Earth and Planetary Science Letters*, *562*, 116879. https://doi.org/10.1016/j.epsl.2021.116879